Enhancement of the Er^{3+} luminescence in Er-doped silica by few-atom metal aggregates

C. Maurizio,[1,2] E. Trave,[3] G. Perotto,[1] V. Bello,[1] D. Pasqualini,[1] P. Mazzoldi,[1] G. Battaglin,[3] T. Cesca,[1] C. Scian,[1] and G. Mattei[1,*]

[1]*CNISM, Department of Physics, University of Padova, via Marzolo 8, I-35131 Padova, Italy*

[2]*CNR-IOM c/o European Synchrotron Radiation Facility, 6 rue J. Horowitz, BP 220, F-38043 Grenoble, France*

[3]*Department of Molecular Sciences and Nanosystems, Ca' Foscari University of Venice, Dorsoduro 2137, I-30123 Venezia, Italy*

(Received 8 November 2010; revised manuscript received 26 February 2011; published 19 May 2011)

The mechanisms of the Er^{3+} photoluminescence enhancement induced by ultrasmall Au nanoclusters (made by less than 20 atoms) incorporated by low-fluence ion implantation into Er-doped silica are discussed. We show that the energy-transfer process from moleculelike Au nanoclusters to the rare-earth ions critically depends on the evolution of the early stages of the Au metal clustering process starting from dispersed or oxidized atoms up to the formation of metal nanometric clusters. This feature has been investigated in detail combining extended x-ray-absorption fine-structure and photoluminescence spectroscopies and using different annealing atmospheres (neutral or reducing) in order to better evidence the chemical with respect to the thermal effect on Au nucleation and growth. We experimentally showed that the enhancement mechanism is improved when the optically active Er ions are coupled to Au clusters composed by 5–10 atoms and it remarkably decreases when the Au cluster size is above 20–30 atoms.

DOI: 10.1103/PhysRevB.83.195430 PACS number(s): 78.55.Qr, 61.46.Bc, 68.55.Ln

I. INTRODUCTION

Metal nanoclusters (NCs) embedded in dielectric matrices are the subject of an increasing number of research works because of the wide range of possible applications in many technological contexts, in particular in nonlinear optics, nanophotonics, and plasmonics.[1] In particular, Au NCs are one of the most investigated systems[2] since they can be considered as a sort of prototype of the metallic behavior at the nanoscale. To this respect, the control of the cluster size distribution and the aggregation state are critical, since the electronic properties strongly depend on the NC's size, so that numerous efforts have been made to control and predict these parameters either during the synthesis process[3,4] or upon suitable post-preparation treatments, such as thermal annealing[5,6] and laser or ion irradiation.[7–10]

More recently, the investigation of the very early stages of metal clustering in a dielectric matrix has attracted much attention also because it has been demonstrated that metal (in particular Au) nanoclusters can enhance under broadband optical excitation the 1.54-μm emission of Er^{3+} ions embedded in a silica matrix.[11,12]

It is well known that the Er^{3+} ion is one of the doping elements of election in the field of optical communication technology,[13,14] since it exhibits a spectroscopically sharp and temperature-stable radiative emission that matches the 1.5-μm minimum loss windows in silica optical fibers.[15] The possibility to improve the rare-earth optical activity through the interaction with suitable fluorescence sensitizers, such as other lanthanides,[16,17] Si,[18–22] or metal[12,23–25] nanostructures, has stimulated the research on a new generation of Er-based near-infrared (NIR) emitting materials for photonic and optoelectronic applications. The comprehension of the basic mechanisms contributing to the sensitization process is of significance in itself, and important for applications. At present, as regards Au NCs, this sensitization (or energy-transfer effect) has been experimentally proved both for large Au clusters (with size of about 20 nm)[11] and for ultrasmall Au structures (size less than 1 nm).[12,26] So, despite the indication from several studies that large clusters are likely not effective in promoting sensitization, it is still not clear whether the cluster size and/or density have a specific role on the Er luminescence efficiency and if other species possibly present in the matrix (i.e., dispersed and/or oxidized Au atoms) can affect the optical properties of the system, as suggested in similar experiments on Ag-mediated energy transfer.[23] Although several papers have investigated the energy-transfer process from metal nanostructures towards rare-earths in glasses, the conclusions on the nature of the sensitizers are generally deduced only indirectly from optical measurements. Our aim is therefore to demonstrate (i) a direct correlation between the number of atoms in the moleculelike Au clusters and the sensitization efficiency by combining synchrotron-based techniques with standard optical characterization, and (ii) that the contribution to PL enhancement from oxidized Au configurations is much less important with respect to that of the reduced (metallic) ones.

In the present work, we produced subnanometric Au NCs in Er-doped silica using a fully ion-beam based approach, in which first Er ions and then Au ions were introduced in the silica matrix by multienergy sequential ion implantation. This technique allows a careful control on the concentration and distribution of the implanted elements within the substrate depth.[1,27,28]

To investigate subnanometric structures and/or metal dispersed in a matrix, the extended x-ray-absorption fine-structure (EXAFS) spectroscopy has been used, since it can detect even clusters made of a few atoms, as well as the possible presence of dopant dispersed into the matrix.[7,29] This challenging investigation allowed us to directly follow the early stages of Au nucleation near the critical radius (for Au, a NC made by 2–3 atoms) and to relate the Au NC size evolution with the Er^{3+} photoluminescence (PL) enhancement.

II. EXPERIMENT

Pure silica slides (Herasil I by Haereus) were doped with Er and Au atoms by sequential ion implantation. To extend the implanted region and to obtain an almost flat concentration profile of the implanted elements, a triple energy implantation sequence is adopted.

As a first step, Er ions were implanted into virgin silica slides at three different energies (50, 100, 190 keV), with current densities of about 0.05 μA/cm^2 and total fluence of $(6.8 \pm 0.9) \times 10^{14}$ Er$^+$/cm^2 [as estimated by Rutherford backscattering spectrometry (RBS)] producing an almost constant Er concentration profile in the implanted region, about 70 nm thick. The Er-implanted slides were then heated for 1 h in N_2 atmosphere at $T = 900$ °C (sample labeled "Er reference") to activate the luminescence of the Er ions, otherwise hindered by the implantation-induced defects. Finally, the Er reference samples underwent a sequence of Au implantations at three different energies (60, 110, 190 keV) to obtain an implanted layer with almost constant Au concentration, overlapped to the Er profile. The Au$^+$ ion-beam current density was about 0.1 μA/cm^2 and the total Au fluence $(6.1 \pm 0.8) \times 10^{15}$ Au$^+$/cm^2 (from RBS), i.e., about ten times the Er fluence.

It is well known that ion implantation produces a wealth of complex defective and/or charged configurations,[30] whose interaction under annealing can influence the chemistry of the system. In the present work we intended to exploit the additional chemical and/or thermal effect of the annealing atmosphere to finely control the nucleation and growth kinetics of the Au clusters. To this aim, co-doped silica slides were then heated at different temperatures up to $T = 900$ °C for 1 h either in reducing atmosphere (forming gas, 5% H_2-95% N_2, labeled "H" in the sample name) or in neutral atmosphere (N_2, labeled "N" in the sample name). The sample labels indicate the heating treatment: e.g., the sample N600 was annealed in neutral atmosphere at $T = 600$ °C whereas the sample H100 was annealed in reducing atmosphere at $T = 100$ °C.

The EXAFS experiment was performed at the Italian beamline GILDA of the European Synchrotron Radiation Facility (Grenoble, France) at the Au L_3 edge. The monochromator was equipped with a couple of (111) Si crystals and the harmonic rejection was achieved by a couple of Pd-coated mirrors, working at an incidence angle of 3 mrad. Due to low Au concentration, the x-ray-absorption spectra were measured in fluorescence mode with a 13-element high-purity Ge detector; the EXAFS spectrum of an Au metallic foil was measured in transmission mode as standard reference; the samples were cooled down at $T = 80$ K to reduce thermal vibrations. The analysis of the EXAFS spectra was performed by the FEFF8-FEFFIT 2.98 package.[31,32] The value of the S_0^2 parameter in the standard EXAFS formula[29] was determined by the analysis of the metallic Au EXAFS spectrum. The Au-O backscattering phase and amplitude were calculated from a Au_2O_3 cluster, while the Au-Au ones were calculated from a Au cluster, providing to extend the calculation for different interatomic distances of the Au-Au couple ($d_{\text{Au-Au}}$), down to $d_{\text{Au-Au}} = 2.68$ Å. The EXAFS signal from the first two coordination shells of atoms around Au was selected by a Fourier filter, then fitted by a multiparameter single scattering fit into the R space (the fitting procedure in k space led to the same results). The Fourier transform range for the spectra of low-temperature-annealed samples was 4–11 Å^{-1}, while for the spectra of high-temperature-annealed silica slides the more intense EXAFS signal allowed a quantitative analysis in a longer range, extended up to 14 Å^{-1}. To reduce the number of the fitting parameters, the mean-square relative displacement (MSRDs) of the Au-O coordination was set to be equal for the different samples, as well as the MSRD of the Au-Au coordination. We have verified that, within the estimated error bars, these constraints do not alter significantly the obtained EXAFS results.

Optical-absorption characterization has been performed with a JASCO V670 spectrophotometer in the 200–900-nm wavelength range. Photoluminescence (PL) investigation was carried out through an experimental setup properly dedicated to the study of the NIR PL activity characterizing the Er ions. Sample excitation was obtained by means of a cw Ar laser, whose pumping lines at 488 and 476.5 nm allow for rare-earth photostimulation, respectively, in resonance (matching the transition between the Er ion $^4I_{15/2}$ ground state and the $^4F_{7/2}$ excited level) and in out-of-resonance conditions (pumping radiation not directly absorbed by the rare-earth). The laser beam had a spot diameter of about 1 mm and it was modulated by a mechanical chopper. A single-grating monochromator provided the spectral discrimination of the luminescence signal, which was detected by a N_2-cooled photomultiplier tube operating in the 1000–1650-nm spectral range. PL emission was acquired with a lock-in amplifier, using the chopper frequency as reference, while data were stored in a PC by a dedicated software. Time-resolved PL analysis was carried out by fixing the detected wavelength and collecting the PL intensity evolution as a function of the time with a transient digitizer (overall time resolution of about 5 μs). PL excitation (PLE) measurements were performed by pumping the samples through a Xe lamp coupled to a monochromator, operating in the 250–800-nm range. Microstructural characterization was performed by transmission electron microscopy (TEM) with a FEI Tecnai Field-emission Gun (FEG) (S)TEM F-20 Super Twin, operating at 200 keV equipped with an EDAX energy-dispersive X-ray spectrometer (EDS), and with scanning deflection coils that allow images to form in the scanning TEM (STEM) mode.

III. RESULTS AND DISCUSSION

A. Structural analysis

The EXAFS spectra recorded at the Au L_3 edge from all the samples are reported in Fig. 1. In the as-implanted sample the main oscillation of the spectrum is strongly damped and has a lower frequency with respect to the bulk Au metallic foil reference. Upon annealing in neutral or reducing atmosphere the typical features of the metallic Au become progressively more visible as the temperature is increased therefore indicating a progressive growth of metal Au nanoclusters. The Fourier transform moduli of all the spectra are reported in Figs. 2(a) and 2(b). For the as-implanted sample, two different coordination distances are present: the first and more evident one is located at $d \simeq 1.5$ Å and is due to an Au-O coordination, while the second one, located in the

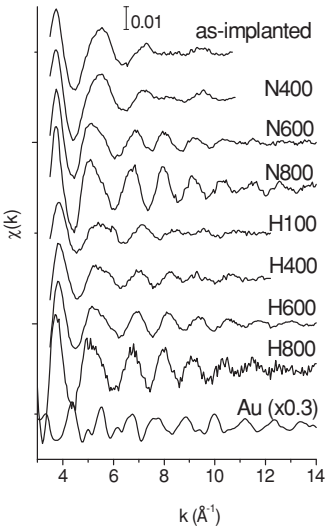

FIG. 1. Au L_3-edge EXAFS spectra of Er-Au-doped silica, compared with an EXAFS spectrum recorded from a metallic Au foil. The spectra are vertically shifted; the scale is labeled.

range $d = 2$–3 Å, is due to a Au-Au metallic coordination related to the presence of Au aggregates. We note here the absence of any significant Au-Er coordination (both in the as-implanted and annealed samples), indicating that Er ions are dispersed into the matrix, without directly (chemically) interacting with Au atoms.

The Au-O coordination is the evidence for a chemical interaction between the implanted Au ions and the silica matrix. Although metal-oxygen interactions are currently found upon implantation of other transition-metal elements,[27,33,34] usually the only coordination found by EXAFS for Au-implanted silica at fluences higher than those used in the present work is the metallic one,[7,35,36] due to the low stability of the Au-O bond [the Gibbs free energy of formation of Au_2O_3 is only 0.078 kJ/mol, to be compared, for example, with 146 kJ/mol for Cu_2O and to 11.2 kJ/mol for Ag_2O (Ref. 37)].

The presence of a dominant Au-O EXAFS signal in the as-implanted samples can be ascribed to the relatively low Au concentration in the silica matrix (not exceeding 2 at. %), so that Au-O interaction is favored with respect to the Au-Au one in the damaged matrix. The concentration of such Au-O bonds has to be reduced to promote and control metal Au NCs nucleation and growth. To this aim, thermal treatments were done in inert or reducing atmosphere to decouple the thermal from the chemical effect on the Au reduction.

Upon heating, as expected, the Au-O coordination progressively fades and becomes undetectable at the highest temperatures investigated (e.g., above 600 °C). Correspondingly, the Au-Au coordination becomes the most relevant signal in the spectra [Figs. 2(a) and 2(b)], indicating that new Au^0 atoms are contributing to the nucleation and growth process of metallic Au nanoclusters. Of course chemistry plays a major role in this process and, while a significant reduction of the Au-O coordination is evident only at or above $T = 600$ °C under N_2 annealing, for heating in forming gas the same effect already occurs at a much lower temperature ($T = 100$ °C).

A systematic EXAFS investigation of this process has been done and in Figs. 2(a) and 2(b) the single scattering fit of the

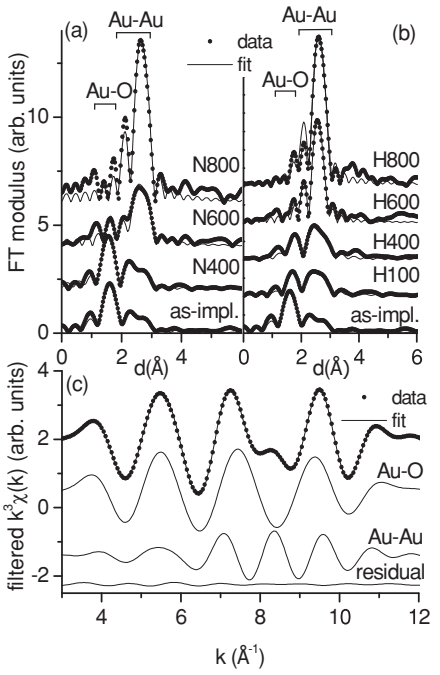

FIG. 2. (a),(b) k^3-weighted Fourier transform moduli and corresponding best-fit curves of the Au-O and Au-Au coordinations of the EXAFS spectra (here the interatomic distance d is not corrected for the backscattering phase shift) upon heating in neutral (a) or reducing (b) atmosphere [the spectrum of the as-implanted sample is reported for clarity in both (a) and (b)]; (c) Fourier-filtered EXAFS spectrum of the as-implanted sample in the range of fitting (solid circles): the corresponding fits (solid line) are superimposed on the data; the residuals and the two single-scattering signals that contribute to the fit are reported.

first two shells (Au-O and Au-Au coordinations) is shown, for all the samples, superimposed to the experimental data. In particular, Fig. 2(c) shows for the as-implanted sample the fit to the experimental filtered signal of the first two coordination shells also in the k space: the single-scattering Au-O and Au-Au signals that contribute to the whole fit are also shown, indicating a dominant contribution of the Au-O correlation.

The results of the EXAFS analysis are summarized in Table I. Consider first the Au-Au coordination shell, which is visible for all the investigated samples. The Au-Au measured coordination distance, $d_{\text{Au-Au}}$, is always lower (of about 3–8%) than the corresponding Au bulk value, $d_{\text{Au-Au}}(\infty) = 2.8840$ Å: this contraction is related to the small size of the Au aggregates and it reflects also in the fact that no appreciable EXAFS signal is found for $d > 3-4$ Å for all the investigated samples. Moreover, only one Au-Au coordination signal is needed in the fitting procedure to reproduce the Au shell, as shown in Fig. 2(c) for the as-implanted sample. This observation indicates that to properly interpret our data we do not need to consider the presence of peculiar structures (e.g., the icosahedral one[39]) of the Au aggregates whose first coordination shell is split into two different interatomic distances.

Due to the lack of reliable experimental measurements of the nanocluster radius R as a function of the nearest-neighbor distance, to have an estimate of the Au nanocluster size

TABLE I. Results of the EXAFS analysis (Au-O and Au-Au first coordination distance) upon annealing in neutral or reducing atmosphere. N is the coordination number, d is the interatomic distance, and σ^2 is the Debye-Waller factor. The crystallographic values for the bulk metallic Au and Au_2O_3 (up to $d = 3.03$ Å) (Ref. 38) are also reported for comparison.

Sample name	N_O	Au-O $d_{Au\text{-}O}$ (Å)	σ^2 ($\times 10^{-4}$ Å^2)	N_{Au}	Au-Au $d_{Au\text{-}Au}$ (Å)	σ^2 ($\times 10^{-4}$ Å^2)
as-impl.	0.9 ± 0.2	2.01 ± 0.02	18 ± 5	1.1 ± 0.2	2.65 ± 0.02	77 ± 15
N400	0.9 ± 0.1	1.97 ± 0.02	18 ± 5	1.4 ± 0.2	2.66 ± 0.01	77 ± 15
N600	0.3 ± 0.1	2.06 ± 0.04	18 ± 5	3.1 ± 1.0	2.77 ± 0.01	77 ± 15
N800				7.0 ± 1.0	2.80 ± 0.01	77 ± 15
H100	0.4 ± 0.1	2.03 ± 0.02	18 ± 5	1.6 ± 0.2	2.66 ± 0.03	77 ± 15
H400	0.4 ± 0.1	2.07 ± 0.02	18 ± 5	2.1 ± 0.2	2.71 ± 0.02	77 ± 15
H600				4.2 ± 0.4	2.73 ± 0.02	77 ± 15
H800				7.1 ± 1.0	2.76 ± 0.02	77 ± 15
Au				12	2.8838	
Au_2O_3	4	1.93-2.07				
	1; 1	2.81; 2.90		1	3.03	

as a function of the annealing process, we transformed the measured Au-Au distances into effective cluster radius R_{eff} according to the following procedure. The first step is to obtain a relationship between the Au nearest-neighbor distance $d_{Au\text{-}Au}$ (output of the EXAFS analysis) and the number of atoms in the clusters, n, while the second one is to relate n with the effective radius R_{eff}. We have therefore compared our EXAFS measured $d_{Au\text{-}Au}$ values with those calculated as a function of n by the state-of-the-art computational approaches available in the literature.

In Fig. 3(a) the average values of $d_{Au\text{-}Au}$ obtained from different calculations based on the density-functional theory,[40–48] or using a tight-binding approach,[49] are reported as a function of the number n of atoms in the Au cluster: each point represents an average of the different calculations for that particular value of n.

These data are quite precisely fitted by a simple size-equation of the form

$$d_{Au\text{-}Au}(n) = d_{Au\text{-}Au}(\infty)\left(1 - \frac{A}{n^B}\right). \quad (1)$$

The obtained best-fit constants are $A = 0.128 \pm 0.009$, $B = 0.37 \pm 0.03$, and the corresponding best-fit curve is shown in Fig. 3(a). It is found that the interatomic distance scales roughly as the inverse cubic root of the number n of atoms in the cluster. We have then used Eq. (1) to estimate n in the Au clusters of the present study. The results are reported in Fig. 3(b): in particular, in the as-implanted sample the average cluster contains 3–4 Au atoms.

It is well known that free metal clusters made by $n < 6$–8 atoms are far from being spherical [linear one-dimensional (1D) or planar 2D configurations are normally found by numerical simulation[50]]. Nevertheless, to give a reasonable estimate of an effective cluster radius R_{eff}, we can assume also for the smallest clusters a spherical geometry, considering that a more compact 3D geometry could be favored by the structural constraint of the silica matrix. Thus as a second step in our approach, R_{eff} can be calculated from the relation $R_{eff} = R_a \sqrt[3]{n}$, where R_a is the average radius of an Au atom in the cluster. As an estimate of R_a we averaged the Au atomic[51] and van der Waals[52] radii, obtaining $R_a = 1.505$ Å.

With this simple procedure we have a sort of calibration curve giving $d_{Au\text{-}Au}$ as a function of R_{eff} and vice versa (the relation being monotonic). The resulting curve is shown in the inset of Fig. 3(a) together with some available experimental results (for its validation) obtained by EXAFS analysis on Au nanoclusters with known size deposited on mylar[53] or stabilized by different ligands.[39,54,55]

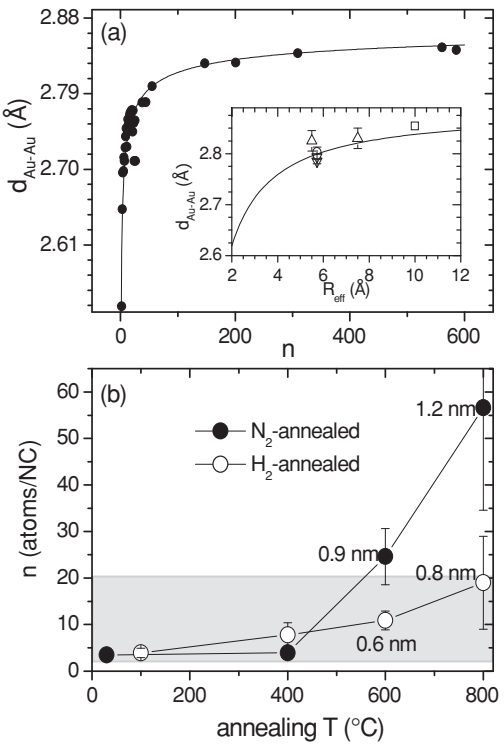

FIG. 3. (a) Average Au-Au nearest-neighbor distance in a Au cluster of n atoms from calculation (average of literature data, filled circles) and best-fit curve (solid line) as in Eq. (1). Inset: average Au-Au nearest-neighbor distance in a Au cluster versus the cluster radius from Eq. (1) and some experimental data from literature (▽, Ref. 39; △, Ref. 53; □, Ref. 54; ◯, Ref. 55). (b) Number n of Au atoms per clusters from the EXAFS analysis as a function of the annealing temperature; the average cluster size is marked near the corresponding data.

With this relation, we compared the Au cluster size in the as-implanted sample to the thermodynamically calculated critical radius for nucleation of a supersaturated solid solution R_c, that is, expressed by $R_c = 2\sigma/|\Delta g_V|$, where σ is the surface free-energy density and Δg_V is the volumetric density of Gibbs free-energy for the formation of the Au bulk phase from gaseous Au. Using $\Delta g_V = 3.22 \times 10^{10}$ J/m^3,[56] and the average values of the literature data for the density of the surface free energy $\sigma = 3.62$ J/m^2,[6,7,57] we obtain $R_c = 2.25$ Å, corresponding to a cluster of 3–4 atoms. This result indicates that in the as-implanted sample we are actually looking at the earliest stage of Au nucleation in which the clusters have the smallest thermodynamically stable size.

For clusters formed by only 3–4 atoms (as in the as-implanted sample, but very similarly also in samples H100 and N400) the expected coordination number for the Au shell, N_{Au}, is about 2–2.5, depending on the cluster structure (triangle or rhombus), with a limiting value of 3 in the case of a four-atom cluster in tetrahedral configuration. If Au atoms are present both in metallic and oxidized form with relative fractions f and $(1-f)$, respectively, the measured N_{Au} is linked to the real one N^*_{Au} by the relation fN^*_{Au}. The number of Au atoms in the Au shell measured for the as-implanted sample is $N_{\mathrm{Au}} = 1.1 \pm 0.2$. Therefore the fraction f of the implanted Au atoms that are in a metallic state is about 40% of the total. Correspondingly, the remaining fraction (i.e., 60%) can be considered as dispersed in the matrix linked to oxygen atoms.

Let us consider first the effect of N_2 annealing. Figure 3 shows in this case that the cluster size remains stable up to $T = 400$ °C (N400 sample), while it increases rapidly up to about 25 atoms (N600) and to 55 atoms (N800), corresponding to a cluster size of about 0.9 ± 0.1 nm and 1.2 ± 0.2 nm, respectively. The growth of the metallic clusters takes place by using the oxidized fraction as a reservoir: indeed, upon heating at $T = 600$ °C the Au-O coordination number decreases by a factor of 3 with respect to the as-implanted sample and is below the EXAFS detectability limit for the N800 sample.

For a cluster of about 25 atoms (sample N600) the expected coordination number of the metal shell is about 6,[58] i.e., two times the EXAFS result in the present work (3.1 ± 1.0), indicating that only about half of the Au atoms form clusters of that size, while half of them are bonded to O atoms in structures similar to those evidenced in the as-implanted sample. Moreover, for the N600 sample the Au-O distance is significantly longer with respect to the as-implanted and N400 samples, suggesting a weaker chemical interaction. In the N800 sample the comparison between the measured (7.0 ± 1.0) and the expected (about 8) coordination number of the metallic shell indicates that the metallic fraction is near 90%, i.e., the oxidized one is about 10%, that is, at limit of the EXAFS sensitivity.

The Au cluster growth has been followed also by TEM analysis. The results are shown in Fig. 4 for the N600, N800, and N900 samples. When Au NCs are made by few atoms, the contrast in the TEM image of the surrounding matrix is sufficient to hinder their visibility. Therefore we could assume a threshold at about $D \sim 0.5$ nm above which an embedded cluster can be detected by TEM. Upon increasing the NC size, as in the N600 sample, it is possible to obtain a more

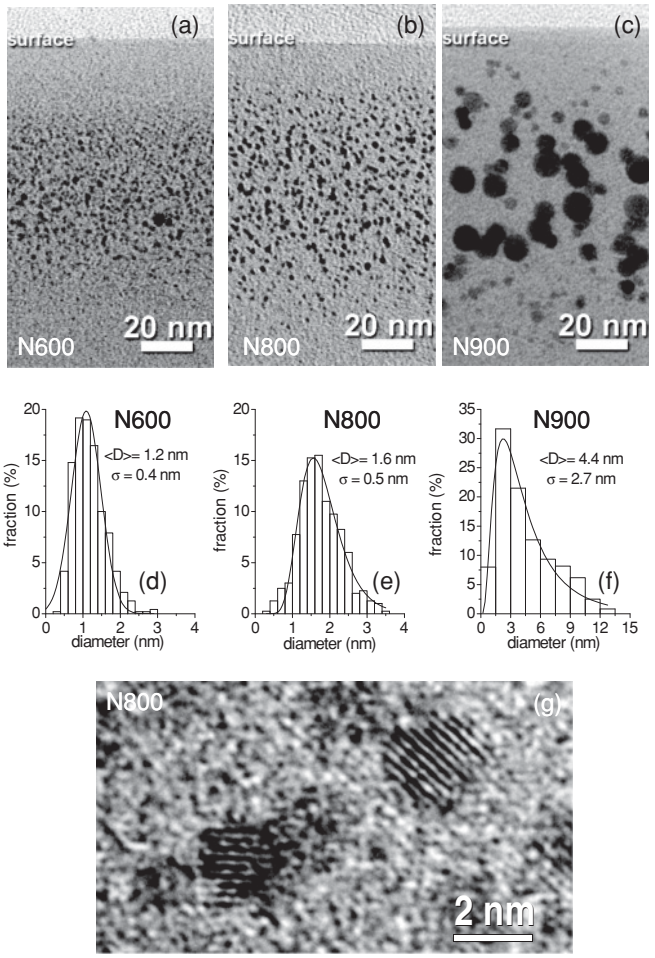

FIG. 4. TEM results on the samples annealed in N_2:(a)–(c) cross-sectional bright-field (BF-TEM) images of the samples N600, N800, N900, respectively, with the corresponding histogram of size distribution (d)–(f). The high-resolution (HR-TEM) image of some Au NCs in sample N800 is shown in (g), with the (111) lattice planes of the fcc phase clearly visible.

reliable histogram of the size distribution, although a possible overestimation can be done by TEM with respect to EXAFS, considering the visibility threshold. Nonetheless, a reasonably good agreement is found between TEM $(1.2 \pm 0.4$ nm) and EXAFS $(0.9 \pm 0.1$ nm). This can be considered as an *a posteriori* support for the use of Eq. (1) to evaluate the cluster size when the TEM data are not accessible.

To speed up the chemical reduction of the Au-O bonds, we performed H_2 annealing in which the chemical and the thermal effects on Au-O interaction are both present. Upon H_2 heating the increase of the cluster size is less pronounced with respect to the N_2 annealing: the average number of atoms in the Au cluster increases from about 3–4 (as-implanted) to about 19 atoms upon heating at 800 °C (corresponding to a cluster size of 0.8 nm). On the contrary, the Au metallic fraction increases faster with respect to the N_2 heating. Indeed, the fraction of atoms that form clusters of the average size indicated in Fig. 3(b) is about 60% for H400, 90% for H600, and 100% for H800 samples, respectively.

To better follow the chemical effect of the annealing atmosphere on the cluster precipitation and growth, Fig. 5(a)

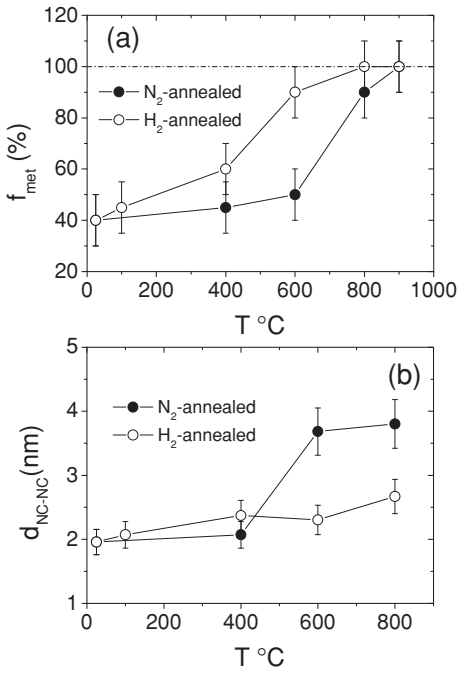

FIG. 5. (a) Fraction of the Au atoms in the metallic (cluster) phase as a function of the annealing atmosphere. (b) average Au intercluster distance $d_{\text{NC-NC}}$.

shows the evolution of the metallic Au fraction as a function of the annealing temperature. The reducing atmosphere annealing determines a significant reduction of the Au-O coordination at a temperature as low as $T = 100$ °C; correspondingly, the coordination number of the Au shell increases with respect to the value of the as-implanted samples, indicating an increase in the average size (see Fig. 3). On the other hand, the Au-O distance increases by increasing the heating temperature (as for the N_2 annealing) indicating a weakening of the Au-O correlation, whose signal falls below EXAFS detectability upon annealing at $T \geqslant 600$ °C: in this case the Au clusters are smaller than upon heating in inert atmosphere at the same temperature and the metal fraction is slightly larger, suggesting a different mechanism for the nucleation and growth.

We remark that the main motivation of the present study is the control of the energy-transfer process from metallic Au nanostructures to emitting Er ions: for this to be tailored, not only the cluster size is relevant but also the average distance between the sensitizer and the emitter plays a significant role. For instance, when the sensitizer is a Si NC, it has been found that a maximum separation of 4–5 nm is required for energy transfer to occur. In the as-implanted sample, assuming an average concentration of 10^{21} Au/cm^3 (as from RBS) and considering just 40% Au atoms in the 3–4-atom metal NCs, we estimate an average cluster numerical density ρ_{NC} of about 0.12 ± 0.03 NC/nm^3, corresponding to an intercluster average distance $d_{\text{NC-NC}}$, of about 2.0 ± 0.2 nm. Therefore for an Er ion concentration of about 10^{20} Er/cm^3 as in the present case, each Au NC is, on average, in interaction with about 1 Er ion within its specific volume (assumed to be a cube of side $d_{\text{NC-NC}}$). RBS and TEM data confirmed that upon annealing the concentration profiles of both Au and Er do not change significantly: therefore from the EXAFS analysis we calculated as a function of the annealing treatment the evolution of $d_{\text{NC-NC}}$ (and correspondingly of ρ_{NC}). The results are shown in Fig. 5(b). We note that up to $T = 800$ °C $d_{\text{NC-NC}}$ is below 4 nm and increases faster for N_2-treated samples.

Consider now the observed cluster growth: in a diffusion-limited aggregation regime the average NC radius R should increase as $R(t)^2 \propto Dt$, where D is the diffusion coefficient and t is the annealing duration:[6] in this condition an Arrhenius plot of $\ln(R_{\text{eff}}^2)$ versus $1/kT$ leads to a linear trend of the data.[5,59] Of course, this regime is progressively substituted by the coarsening one (Ostwald ripening regime) in which the larger and thermodynamically more stable clusters grow at the expense of the smaller ones producing a net decrease of the NC density. This regime definitely dominates when there are no longer Au atoms to be reduced from the "oxide state" reservoir. If we compare in Fig. 3(b) the rate of NC size growth in both annealing atmospheres, while the H_2-annealed samples show a modest increase, the N_2-annealed ones show a remarkable discontinuity and a fast growth rate above $T = 400$ °C. This can be the signature of the onset of a different growth regime.[6] Moreover, if we analyze with the Arrhenius plot the cluster size in the samples heated in inert atmosphere from 400 to 800 °C an activation energy E_a of about 0.28 eV/atom is found, to be compared with a value of 2.14 eV/atom measured for Au diffusion in silica.[60] To properly interpret these results, one has to take into account both the diffusion-controlled regime, almost independent of the annealing atmosphere and dominating at $T \leqslant 400$ °C, and the coarsening one, which is active at higher temperatures and much more chemistry dependent. Indeed, below 400 °C it has already been suggested that the modest dependence of cluster size on the temperature is due to a diffusion mechanism controlled mainly by the implantation radiation damage.[5] Upon inert atmosphere annealing, the reduction of Au atoms occurs at (or above) $T = 400$–600 °C, i.e., when the Au diffusion coefficient is expected to be sufficiently high: in this condition the newly reduced Au atoms can diffuse more easily and instead of locally nucleating new embryos prefer to feed already formed and thermodynamically more stable clusters, increasing very rapidly their average size. This in turn ends up in a cluster density ρ_{NC}, which drops above 600 °C due to the dominating coarsening regime. On the contrary, by switching on the chemical effect of the H_2 annealing, it is possible to speed up the Au-O bond breaking rate already between 100 and 400 °C. Nevertheless, the diffusivity of the Au atoms at these temperatures is still insufficient to produce an evident increase of the NC size. On the other hand, the availability of reduced Au atoms promotes the development of new nucleation embryos, which compensate more effectively at higher temperatures (i.e., above 400 °C), the decrease of ρ_{NC} typical of the Ostwald ripening observed during inert annealing. As a net result, the NC density is higher for N_2-annealed samples below $T = 600$ °C and lower above, with respect to the H_2-annealed ones.

As will be described in the next section, this structural evolution and the different chemistry triggered by the annealing atmosphere will give interesting insights in the comprehension

of the mechanisms of energy transfer from the Au NCs to the emitting rare-earth ions.

B. Photoluminescence properties

From the PL spectra of Fig. 6(a), obtained by pumping at 488 nm with a cw Ar laser, we observe that Au co-implantation on Er-doped matrix followed by annealing at 600 °C in either reducing or oxidizing atmosphere induces a manifest enhancement of the characteristic PL emission at 1.5 μm related to the Er^{3+} $^4I_{13/2} \rightarrow {}^4I_{15/2}$ transition in silica. With respect to the Er reference, we measured an increase of the integrated PL signal by six to seven times for N600 and by about four times for H600, respectively. As already reported in Ref. 12, Er sensitization reaches its maximum level upon a heat treatment in this temperature range in virtue of an adequate recovery of the optical quality for the implantation-damaged matrix and of a finely tuned control of the metal aggregation process determining the formation of Au-related sensitizing centers. Furthermore, Fig. 6(b) shows that, whereas no PL signal is revealed in the Er reference sample under nonresonant excitation at 476.5 nm, an even further increase of the PL emission intensity at 1.5 μm occurs for both N600 and H600, indicating the occurrence of an Au-mediated energy-transfer process.

Interesting considerations concerning the mechanism responsible for the observed PL enhancement can be derived from the excitation spectra shown in Fig. 7, related to the pumping wavelength dependence of the PL emission signal at 1540 nm. Unlike the Er reference, which shows some of the typical resonance features related to the Er^{3+} absorption levels, both N600 and H600 samples exhibit an excitation profile characterized by a monotonic increase toward the UV that covers the whole visible range. This remarkable modification of the PL excitation spectrum was already observed for systems where Er ions are included in a matrix co-doped with either metal[23,24] or Si nanoclusters,[18,19,22] and it is commonly

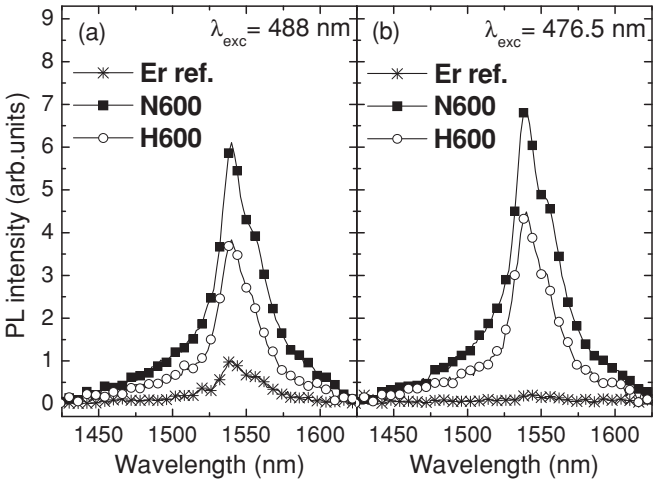

FIG. 6. Comparison of Er PL spectrum around 1.5 μm among the Er reference and the co-doped samples heated at 600 °C in inert (N600) and reducing (H600) atmospheres under 488 nm resonant (a) or 476.5 nm nonresonant (b) excitation. The PL intensity maximum of the Er reference sample is normalized to 1 and rescaled accordingly for the co-implanted samples.

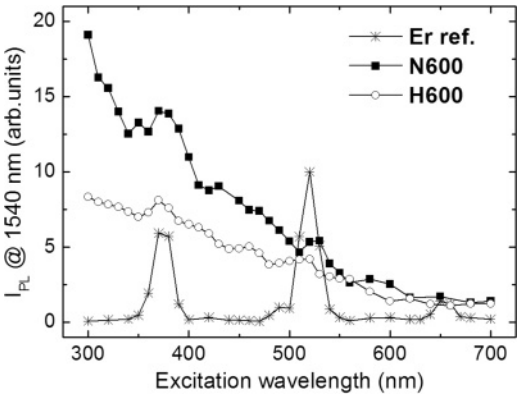

FIG. 7. PL excitation spectra measured at 1540 nm for the Er reference and the co-doped samples annealed at 600 °C. Er ion optical pumping was carried out using a 150-mW Xe lamp coupled with a monochromator. Intensity scale has been calibrated by the PL measurements performed under the 488-nm Ar laser excitation.

recognized as a fingerprint of the occurrence of an energy transfer toward the Er ions driven by the optically active co-dopants (e.g., metal or Si nanoclusters). Therefore also in the present case of co-doped glasses the Au implantation induces the opening of a new Er photostimulation channel, triggered by the metal sensitizer, which efficiently absorbs light and promotes a consequent transfer mechanism to the rare-earth. Moreover, this nonresonant excitation results to be dominant with respect to the direct, resonant, Er^{3+} excitation.

The difference in the Er^{3+} PL intensity between the two annealing atmospheres is a hint that the chemical effect on the Au clustering plays a relevant role in triggering the efficiency of the energy-transfer process. This can be further understood by considering the temperature evolution of the PL signal under in- and out-of-resonance pumping, shown in Fig. 8.

The first observation is that only minor differences can be evidenced between the curves in Fig. 8(a) (nonresonant excitation) and Fig. 8(b) (resonant excitation), confirming that the Er^{3+} radiative relaxation is dominated by the nonresonant Au-mediated excitation path. Moreover, already the untreated Au co-doped sample exhibits a normalized PL intensity slightly larger than that of the Er reference sample: this indicates that the sensitization effect is still active without further recovery of the matrix.

Moreover, the thermal evolution of the PL intensities shown in Fig. 8(a) is characterized by a maximum at $T = 600$ °C for both annealing atmospheres, followed by a rapid decrease in the PL intensity evidently due to a decreased efficiency of the energy-transfer process above 600 °C. This result should be unexpected considering the uniquely beneficial thermal effect on the Er environment, which is known to occur in silica up to 900–1000 °C under inert atmosphere annealing.[14] Therefore other phenomena should occur together to produce the observed behavior in Fig. 8, and this result can be consistently interpreted on the basis of the EXAFS results about the Au clustering as a function of the heat treatments. In particular, we can consider the following concomitant mechanisms: (i) the recovery of the matrix damaged by Au implantation, (ii) the chemical effect of the reducing atmosphere on the Er emitting site, and (iii) the thermally

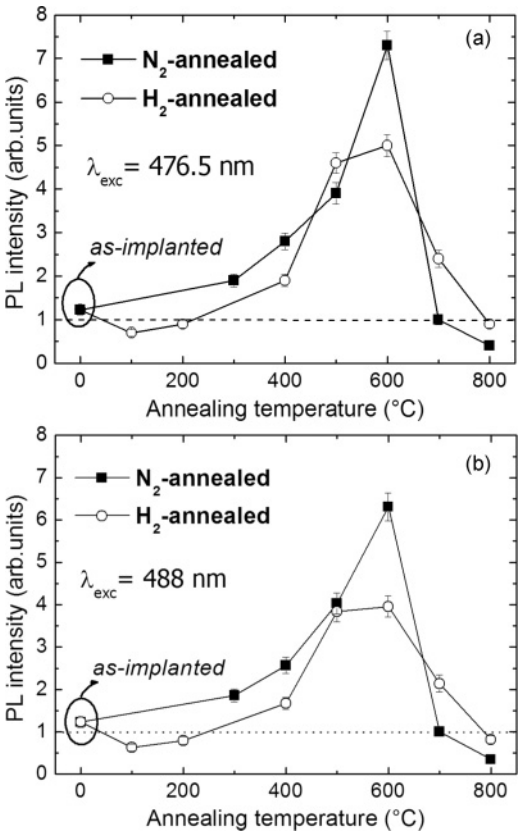

FIG. 8. Evolution of PL emission at 1.5 μm as a function of the annealing temperature in reducing or inert atmosphere for the co-doped samples optically excited nonresonantly at 476.5 nm (a) and resonantly at 488 nm (b). The intensity values are normalized to the Er reference PL spectrum (set to 1).

and chemically activated Au clustering. Concerning the first effect, it is well known that implantation-generated defective sites can interact with the Er ions promoting the activation of nonradiative de-excitation channels with a reduction of the excited-state lifetime (and hence of the PL efficiency) for the rare-earth optical emission.[14] Also the Er local coordination environment can be influenced by the passivating effect of the reducing atmosphere, possibly influencing the reconstruction of the octahedral oxygen coordination required by the Er^{3+} ion for an optimal PL emission.[61] Considering that the beneficial effect of the Er site reconstruction and of the annealing of the radiation induced damage tends to improve the PL emission, we should expect a continuous increase with the temperature of the nonresonant PL emission. On the contrary, the observed decrease of the PL intensity (at different rates for the two annealing atmospheres) requires the onset of the third process: in the temperature range between 600 and 800 °C the clustering of Au atoms proceeds faster and produces, together with the increase of the Au cluster size (as shown in Figs. 3 and 4) in an Ostwald ripening regime, also a decrease of the cluster volumetric fraction with a corresponding reduction of the number of Au-related sensitizing agents [see Fig. 5(b)]. Directly linked to this clustering is the reduction of the oxidized fraction, which obviously goes faster in the sample annealed under reducing atmosphere. This point is particularly relevant to assess the nature of the sensitizer: it is the Au metallic fraction f_{met} and not the oxidized one that is able to make the energy-transfer process. Indeed, as we have obtained from the EXAFS analysis (see Fig. 5), f_{met} is about 90% for the H600 sample and the nonresonant PL intensity is at its maximum. Moreover, at 700 °C the PL enhancement factor for the H700 sample is still about 2.5 while f_{met} practically reached the totality of the Au atoms. Therefore the reduction of the PL intensity should be ascribed to the Au metal cluster growth (whose dynamics is dependent on the annealing atmosphere): when the Au cluster size becomes larger than a certain threshold, the electronic structure of the sensitizer changes and the optimal energy transfer is progressively lost. This is reasonably understood considering that the subnanometric moleculelike Au cluster undergoes a progressive closure of the highest occupied molecular orbital–lowest unoccupied molecular orbital gap as the number of atoms increases, with the progressive onset of the bulklike metallic behavior. Further support to this conclusion comes from the already mentioned nucleation and growth evolution of Au clusters as a function of the annealing atmosphere. Indeed, during the thermal treatments in inert atmosphere the nucleation can start only at higher temperatures due to the lack of the chemical effect in breaking the Au-O bonds, which on the contrary starts at lower temperatures under reducing atmosphere and is still active at higher temperatures where new clusters can nucleate. This ends up in the slower growth rate of the average Au cluster size under reducing atmosphere observed in Fig. 5, and correspondingly to a broader size distribution. Therefore by correlating the PL with the EXAFS results and assuming a sharper size distribution for the reducing atmosphere annealing, we can conclude that the most efficient Au moleculelike sensitizers are made of 3–20 Au atoms, as indicated by the gray band in Fig. 3(b). The less efficient PL emission of H600 with respect to N600 could be also due to a detrimental effect of the reducing atmosphere annealing on the Er octahedral environment site reconstruction.[61]

Moreover, the structural and optical analyses show that the average Er-Au cluster distance in the samples where the PL intensity is highest (N600 and H600) is less than 4 nm, indicating that the maximum Er sensitizer distance that allows the transfer of energy is around or above this value. To investigate this point we have measured the lifetime of the PL emission. Figure 9 reports a comparison between the 1540-nm PL decay transients for the co-doped samples annealed at 600 °C, in both inert and reducing atmospheres, and the Er reference. The main evidence is that the curves for the co-implanted glasses follow a nonexponential trend, which can be well described by a stretched exponential function of the form

$$I_{\mathrm{PL}}(t) = I_{\mathrm{PL}}(0)\exp\left[-\left(\frac{t}{\tau}\right)^{\beta}\right], \qquad (2)$$

where τ is the PL lifetime and β represents the stretching factor, which ranges between 0 and 1. It is worth considering that this kind of transient behavior is observed for all the investigated samples and that this effect can be related to some inhomogeneities in the Er ion environment after Au incorporation, giving a larger distribution in the probability for the de-excitation process. Therefore the β

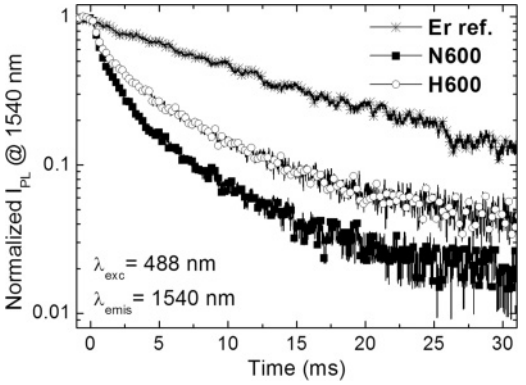

FIG. 9. Time-resolved curves related to the PL signal at 1540 nm for the Er and Au co-implanted samples heated at 600 °C in inert (N600) and reducing (H600) atmospheres.

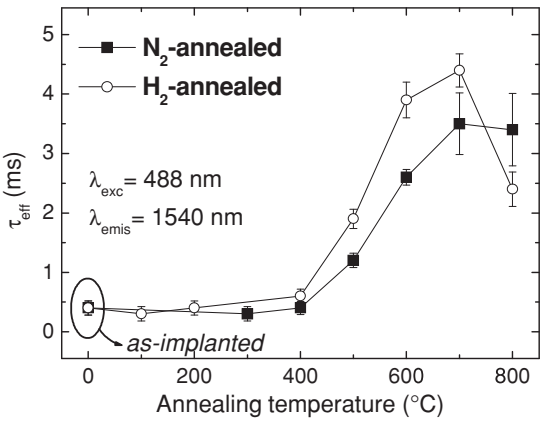

FIG. 10. Evolution of the effective lifetime τ_{eff} as a function of the annealing temperature in reducing or inert atmosphere for the co-doped samples resonantly excited at 488 nm.

factor quantifies the dispersion in the relaxation rate and the observed time-resolved PL curves account for the different excited-state lifetimes characterizing all the optically active Er ions.

Nevertheless, to characterize each sample with an average τ value, we define an effective lifetime τ_{eff} to characterize the PL dynamics for the co-doped systems:

$$\tau_{eff} = \frac{1}{I_{PL}(0)} \int_0^\infty I_{PL}(t)dt = \frac{\tau}{\beta} \Gamma\left(\frac{1}{\beta}\right), \tag{3}$$

where $I_{PL}(t)$ is the luminescence intensity as a function of time. According to Eqs. (2) and (3) and considering the definition of the $\Gamma(x)$ function, τ_{eff} can be determined from the fitting parameters τ and β.

From the analysis of the time-resolved PL curves of Fig. 9, for N600 and H600 samples we have determined a τ_{eff} value of 2.6 ± 0.2 ms and 3.9 ± 0.3 ms, respectively, to be compared with a lifetime of 12.7 ± 0.2 ms for the Er reference (for which $\beta = 1$, i.e., a single exponential decay). A lifetime reduction of the $^4I_{13/2}$ excited state for Er^{3+} ions in silica is commonly observed after co-dopant incorporation, as for glasses containing rare-earth ions and Si (Ref. 62) or metallic species.[23,24] This shortening effect can be ascribed to the activation of fast nonradiative de-excitation channels as a consequence of Au co-implantation, or to the increase of the radiative rate for $^4I_{13/2}$ excited-state relaxation due to a modification on the refractive index of the co-doped matrix.[63]

The temperature evolution of the τ_{eff} is shown in Fig. 10. For both annealing conditions the lifetime increases with temperature due to the progressive matrix recovery, with a parallel enhancement of the 1.5-μm PL signal. This result further supports the proposed mechanism for the moleculelike mediated energy transfer: indeed, the decrease in PL intensity above 600 °C cannot be ascribed to Er (whose emission properties are on the contrary improved by the annealing), but to the growth of the Au NCs above the efficiency threshold for sensitization, promoting a decoupling between sensitizers and emitting ions. On the other hand, upon 800 °C annealing in reducing atmosphere a lifetime reduction takes place. Even though this evidence needs further exploration, in principle we can link it to Er clustering effects or hydrogen-passivation of the emitting centers with a consequent PL efficiency decrease.

An important parameter associated to the efficiency of the energy-transfer mechanism is the effective cross section σ_{eff} for the Er ion excitation mediated by the Au-related sensitizers. Thus following a phenomenological model fruitfully adopted for describing the Er sensitization through Si nanoclusters,[19,22,64] we can estimate σ_{eff} for the Er reference and for the co-doped samples from the risetime intensity as[19]

$$I_{PL}(t) = I_{PL}^S \left[1 - \exp\left(-\frac{t}{\tau_{on}}\right)\right], \tag{4}$$

where I_{PL}^S represents the steady-state PL intensity, and τ_{on} is the PL rise time defined as

$$\frac{1}{\tau_{on}} = \sigma_{eff}\phi + \frac{1}{\tau} \tag{5}$$

with σ_{eff} the Au-mediated effective cross section for the Er ion excitation, ϕ the photon flux of the optical pumping source, and τ the excited-state lifetime. Hence the effective excitation cross section can be estimated by evaluating the τ_{on} dependence on the pumping photon flux ϕ, as shown in Fig. 11 for the N600 sample (the inset reports three rise-time curves collected in the explored pumping power range).

The inverse of the rise time exhibits a linear increase with the pumping photon flux, while at higher laser flux a saturation effect takes place. Therefore for estimating the Er^{3+} effective cross section σ_{eff} we restricted to the linear (i.e., low flux) region of the plot obtaining a value of $(4.7 \pm 0.8) \times 10^{-17}$ cm^2.

It is worth underlining that this σ_{eff} value is about three orders of magnitude higher than the absorption cross section typically measured in this wavelength range for Er embedded in dielectrics.[13] Therefore this evidence clearly demonstrates that the 1.5-μm PL enhancement is due to a remarkable increase in the efficiency of the Au-mediated excitation path. The same procedure was also adopted for the H600 sample, providing a σ_{eff} value of $(1.4 \pm 0.3) \times 10^{-17}$ cm^2. Hence even in this case we observe a manifest increase of the optical

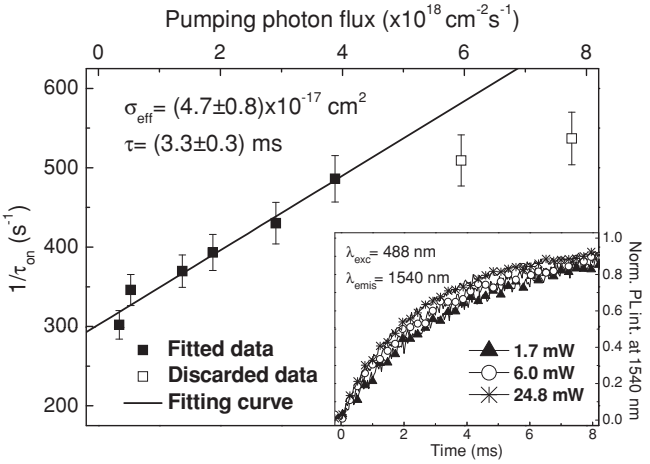

FIG. 11. Evolution of $1/\tau_{on}$ (the inverse of the rise time) as a function of the exciting photon flux, estimated from the 1540-nm PL rising curves taken on the N600 sample. The continuous line is a linear fit of the experimental points for the evaluation of σ_{eff} by means of Eq. (5). Inset: typical time evolution of the PL rising signal normalized to the steady-state emission and taken at 1540 nm upon 488 nm excitation at the reported pumping laser powers.

pumping yield for rare-earth stimulation due to a remarkable enhancement of the overall excitation cross section.

IV. CONCLUSION

We have investigated the mechanisms of the 1.54-μm Er^{3+} photoluminescence emission enhancement in Er + Au implanted silica triggered by moleculelike Au clusters by studying the very early stages of the Au cluster nucleation and growth. EXAFS spectroscopy allowed us to detect the formation of Au clusters with size 3–4 atoms, i.e., close to the critical one, as produced by the Au ion implantation process, as well as their evolution upon selected annealing treatments: the chemical effect of the annealing atmosphere allowed us to finely control the dynamics of the cluster growth. It is found that Au aggregates of few atoms are efficient sensitizers for the Er^{3+} photoluminescence emission and that the efficiency of the energy-transfer process is strongly dependent on the cluster size. The most efficient Au-related sensitizers are very small Au clusters, made of 3–20 atoms, showing that the corresponding energy transfer is not mediated by the surface plasmon resonance of the metal clusters nor by oxidized Au configurations. In particular, in presence of 10–20 Au atom clusters (samples annealed at 600 °C), the estimated effective cross section for the Er ion excitation is $\sim 10^{-17}$ cm^2, i.e., about three orders of magnitude larger than that of pure Er^{3+}. Upon annealing at higher temperature a further cluster growth determines a progressively less efficient energy transfer from the Au cluster to the Er ions with a corresponding decrease of the PL intensity, despite a still relatively long photoluminescence lifetime.

*giovanni.mattei@unipd.it

[1] P. Mazzoldi and G. Mattei, in *Metal Nanoclusters in Catalysis and Materials Science: The Issue of Size-Control*, edited by B. Corain, G. Schmid, and N. Toshima (Elsevier, Amsterdam, 2007), pp. 281–303.

[2] M.-C. Daniel and D. Astruc, Chem. Rev. **104**, 293 (2004).

[3] G. Kellermann and A. F. Craievich, Phys. Rev. B **70**, 054106 (2004).

[4] E. Valentin, H. Bernas, C. Ricolleau, and F. Creuzet, Phys. Rev. Lett. **86**, 99 (2001).

[5] A. Miotello, G. De Marchi, G. Mattei, P. Mazzoldi, and C. Sada, Phys. Rev. B **63**, 075409 (2001).

[6] G. De Marchi, G. Mattei, P. Mazzoldi, C. Sada, and A. Miotello, J. Appl. Phys. **92**, 4249 (2002).

[7] P. Kluth, B. Johannessen, G. J. Foran, D. J. Cookson, S. M. Kluth, and M. C. Ridgway, Phys. Rev. B **74**, 014202 (2006).

[8] K. H. Heinig, T. Mueller, B. Schmidt, M. Strobel, and W. Moeller, Appl. Phys. A **77**, 17 (2003).

[9] G. Battaglin *et al.*, Nucl. Instrum. Methods Phys. Res., Sect. B **175-177**, 410 (2001).

[10] G. Battaglin *et al.*, Nucl. Instrum. Methods Phys. Res., Sect. B **200**, 185 (2003).

[11] M. Fukushima, N. Managaki, M. Fujii, H. Yanagi, and S. Hayashi, J. Appl. Phys. **98**, 024316 (2005).

[12] E. Trave, G. Mattei, P. Mazzoldi, G. Pellegrini, C. Scian, C. Maurizio, and G. Battaglin, Appl. Phys. Lett. **89**, 151121 (2006).

[13] W. Miniscalco, J. Lightwave Technol. **9**, 234 (1991).

[14] A. Polman, J. Appl. Phys. **82**, 1 (1997).

[15] S. Hüffner, *Optical Spectra of Transparent Rare-Earth Compounds* (Academic, New York, 1978).

[16] F. Auzel, Phys. Rev. B **13**, 2809 (1976).

[17] C. Strohhöfer and A. Polman, Opt. Mater. **21**, 705 (2003).

[18] M. Fujii, M. Yoshida, Y. Kanzawa, S. Hayashi, and K. Yamamoto, Appl. Phys. Lett. **71**, 1198 (1997).

[19] G. Franzò, V. Vinciguerra, and F. Priolo, Appl. Phys. A **69**, 3 (1999).

[20] P. G. Kik, M. L. Brongersma, and A. Polman, Appl. Phys. Lett. **76**, 2325 (2000).

[21] D. Pacifici, G. Franzò, F. Priolo, F. Iacona, and L. Dal Negro, Phys. Rev. B **67**, 245301 (2003).

[22] F. Enrichi *et al.*, J. Appl. Phys. **96**, 3925 (2004).

[23] C. Stronhhöfer and A. Polman, Appl. Phys. Lett. **81**, 1414 (2002).

[24] A. Martucci *et al.*, Appl. Phys. A **80**, 557 (2004).

[25] M. Mattarelli, M. Montagna, K. Vishnubhatla, A. Chiasera, M. Ferrari, and G. C. Righini, Phys. Rev. B **75**, 125102 (2007).

[26] M. Eichelbaum and K. Rademann, Adv. Funct. Mater. **19**, 2045 (2009).

[27] G. Mattei, C. Maurizio, P. Mazzoldi, F. D'Acapito, G. Battaglin, E. Cattaruzza, C. de Julian Fernandez, and C. Sada, Phys. Rev. B **71**, 195418 (2005).

[28] P. Mazzoldi, G. Mattei, C. Maurizio, E. Cattaruzza, and F. Gonella, *Optical Science and Engineering*, Vol. 95 (Taylor and Francis, CRC Press, London, 2005).

[29] J. J. Rehr and R. C. Albers, Rev. Mod. Phys. **72**, 621 (2000).

[30] R. Espiau de Lamaestre, H. Béa, H. Bernas, J. Belloni, and J. L. Marignier, Phys. Rev. B **76**, 205431 (2007).

[31] A. Ankudinov, B. Ravel, J. J. Rehr, and M. Newville, FEFFIT manual within the FEFF project, University of Washington, Seattle, USA, 1992-1999.
[32] A. L. Ankudinov, B. Ravel, J. J. Rehr, and S. D. Conradson, Phys. Rev. B **58**, 7565 (1998).
[33] F. D'Acapito, S. Mobilio, F. Gonella, C. Maurizio, P. Mazzoldi, G. Battaglin, E. Cattaruzza, and F. Zontone, Eur. Phys. J. D **10**, 123 (2000).
[34] S. Spiga, R. Mantovan, M. Fanciulli, N. Ferretti, F. Boscherini, F. D'Acapito, B. Schmidt, R. Grötzschel, and A. Mücklich, Phys. Rev. B **68**, 205419 (2003).
[35] C. Maurizio, F. Gonella, E. Cattaruzza, P. Mazzoldi, and F. D'Acapito, Nucl. Instrum. Methods Phys. Res., Sect. B **200**, 126 (2003).
[36] C. Maurizio, G. Mattei, P. Mazzoldi, S. Padovani, E. Cattaruzza, F. Gonella, F. D'Acapito, and F. Zontone, Nucl. Instrum. Methods Phys. Res., Sect. B **200**, 178 (2003).
[37] D. Lide, *CRC Handbook of Chemistry and Physics*, 85th ed. (CRC, Boca Raton, 2004).
[38] P. G. Jones, H. Rumpel, E. Schwarzmann, and G. M. Sheldrick, Acta Crystallogr. Sect. B **35**, 1435 (1979).
[39] R. E. Benfield, D. Grandjean, M. Kröll, R. Pugin, T. Sawitowski, and G. Schmid, J. Phys. Chem. B **105**, 1961 (2001).
[40] J. Wang, G. Wang, and J. Zhao, Chem. Phys. Lett. **380**, 716 (2003).
[41] G. Bravo-Perez, I. Garzon, and O. Novaro, J. Mol. Struct. **493**, 225 (1999).
[42] I. L. Garzon, K. Michaelian, M. R. Beltran, A. Posada Amarillas, P. Ordejon, E. Artacho, D. Sanchez-Portal, and J. M. Soler, Phys. Rev. Lett. **81**, 1600 (1998).
[43] O. D. Häberlen, S. Chung, M. Stener, and N. Rösch, J. Chem. Phys. **106**, 5189 (1996).
[44] E. M. Fernandez, J. M. Soler, I. L. Garzon, and L. C. Balbas, Phys. Rev. B **70**, 165403 (2004).
[45] J. Wang, G. Wang, and J. Zhao, Phys. Rev. B **66**, 035418 (2002).
[46] W. Fa, C. Luo, and J. Dong, Phys. Rev. B **72**, 205428 (2005).
[47] C. Majumder and S. K. Kulshreshtha, Phys. Rev. B **73**, 155427 (2006).
[48] H. Häkkinen and U. Landman, Phys. Rev. B **62**, R2287 (2000).
[49] A. Pinto, A. R. Pennisi, G. Faraci, G. D'Agostino, S. Mobilio, and F. Boscherini, Phys. Rev. B **51**, 5315 (1995).
[50] V. Bonačić-Koutecký, J. Burda, R. Mitrić, M. Ge, G. Zampella, and P. Fantucci, J. Chem. Phys. **117**, 3120 (2002).
[51] J. C. Slater, J. Chem. Phys. **41**, 3199 (1964).
[52] A. Bondi, J. Phys. Chem. **68**, 441 (1964).
[53] A. Balerna, E. Bernieri, P. Picozzi, A. Reale, S. Santucci, E. Burattini, and S. Mobilio, Phys. Rev. B **31**, 5058 (1985).
[54] D. Zanchet, H. Tolentino, M. C. Martin Alves, O. L. Alves, and D. Ugarte, Chem. Phys. Lett. **323**, 167 (2000).
[55] M. A. Marcus, M. P. Andrews, J. Zegenhagen, A. S. Bommannavar, and P. Montano, Phys. Rev. B **42**, 3312 (1990).
[56] O. Knacke, O. Kubashewski, and K. Hesselmann, *Thermochemical Properties of Inorganic Substancies* (Springer, New York, 1991).
[57] A. Balerna, E. Bernieri, P. Picozzi, A. Reale, S. Santucci, E. Burattini, and S. Mobilio, Surf. Sci. **156**, 206 (1985).
[58] J. Löffler and J. Weissmüller, Phys. Rev. B **52**, 7076 (1995).
[59] I. Lifshitz and V. Slezof, Zh. Eksp. Teor. Fiz. **35**, 479 (1958).
[60] R. Collins, D. K. Schroder, and C. T. Sah, Appl. Phys. Lett. **8**, 323 (1996).
[61] C. Maurizio, G. Perotto, G. Mattei, E. Trave, and P. Mazzoldi, Nucl. Instrum. Methods Phys. Res., Sect. B **268**, 3215 (2010).
[62] M. Wojdak, M. Klik, M. Forcales, O. B. Gusev, T. Gregorkiewicz, D. Pacifici, G. Franzò, F. Priolo, and F. Iacona, Phys. Rev. B **69**, 233315 (2004).
[63] E. Snoeks, A. Lagendijk, and A. Polman, Phys. Rev. Lett. **74**, 2459 (1995).
[64] A. J. Kenyon, C. E. Chryssou, C. W. Pitt, T. Shimitzu Iwayama, D. E. Hole, N. Sharma, and C. J. Humphreys, J. Appl. Phys. **91**, 367 (2002).